Heritage Science

RESEARCH

Open Access

Visualizing water seepage dynamics in grotto relics via atom-based representative model

Junxia Wang*

Abstract

Water seepage in grotto relics, i.e., Yungang Grottoes, Dazu Rock Carvings, is a key issue to accurately describe the deterioration and weathering process of grotto rock mass. Considering rainfall infiltration, Finite element simulation was performed for studying the water flow through macro-channel of fractured rock in the 4th cave of Yungang Grottoes, where a group of joints with directions of S62°E and N5°W are widely developed. A 3D atom-based representative model was derived from X-ray diffraction (XRD) patterns and the related semi-quantitative calculation of grotto rock powders, for visualizing the associated seepage characteristics through micro-channel by means of molecular dynamics simulation, for the first time. By analyzing various properties, ranging from the configuration and energetic behaviors to the dynamic characteristics, the calculated water flux and mass flow rate were equal to 270 ns^{-1} and 8.10×10^{-12} g s^{-1}, respectively. A dynamic process of water transport from the entrance region to the exit region was examined and it is consistent with the relative concentration profiles at the corresponding stage. The tagged O atoms experienced a zigzag movement instead of linear motion as expected, roughly exhibited the same target direction. The seepage characteristics in grotto relics experienced a complex evolution process and three types can be summarized: water infiltrates through micro-channels with a low flow rate; it flows through fracture with a relatively high flow rate; it turned into a kind of analogous pipe flow in inter-connected fracture network, resulting in water seepage hazard. Current simulation studies provide helpful insights for understanding the water flow-infiltration behavior of fractured rock in grotto relics.

Keywords Transport dynamics, Seepage channel, Grotto relics, Atom-based model

Introduction

Grotto relics in China are widely distributed with the unique artistic features and historical value. As a global tangible cultural heritage, Yungang Grottoes and Dazu Rock Carvings have been inscribed into the World Heritage List by the United Nations Educational, Scientific and Cultural Organization (UNESCO) [1–3]. However, in the past few decades, the Grotto cultural relics have experienced different degrees of damage due to the long-term adverse effects of natural forces, human influences and environmental erosion, among which water seepage and weathering were responsible for the terrible deterioration and greatly threaten to the conservation of grotto relics in China [4–6]. Affected by complex geological structures and hydrological conditions, they have been a serious challenge. Previous studies indicated that water is one of the main causes of weathering to the grottoes and the phenomena such as swelling, disintegration and softening occurred after the water penetrated and interacted with the rock, resulting in the reduction of stability. The various forms of occurrence and special action

*Correspondence:
Junxia Wang
jxwang@whrsm.ac.cn
State Key Laboratory of Geomechanics and Geotechnical Engineering, Institute of Rock and Soil Mechanics, Chinese Academy of Sciences, Wuhan 430071, China

of slight seepage produced a cyclical effect to the Grotto rock mass, and turned to be a dominant factor, accelerating the deterioration and weathering destruction of rock mass [7–11]. The existence of fracture network usually functions as an underground water flow path, thus posing a serious threat to safety of grotto relics. Therefore, the formation and mechanism of water seepage of fractured rock in grotto relics is a key issue to accurately describe the erosion and weathering process.

Fluid flow through macro-scale channels, i.e., faults, joints, fracture and so on, is crucial for evaluating the stability of geotechnical engineering and the mechanical behaviors in rock mass because they are recognized as the main channel for water migration. The finite element (FE) method and finite difference (FD) method were commonly used methods in solving complex problems in seepage mechanics and engineering, evolving from the seepage path, seepage process to hydraulic fracturing and coupling implementation [12–16]. The FE and FD method proved successful in evaluating water seepage from macro-scale, but there is little relevant research associated with the water seepage of fractured rock in grotto relics. Furthermore, the flow process among micro-channels associated with H_2O molecules migration was ignored.

Fluid flow through micro-scale channels (small pores), driven by external fields, is critical to many fields of application, i.e., membrane separation, drug delivery, sensors, fuel cells, gas separation, desalination and so on [17–22]. Molecular dynamics (MD) simulation has been proved to be an efficient technique to simulate microscopic motions of molecules based on the known physics and the interactions between the molecules [23–25]. Using molecular dynamics approach, it was able to tackle the question of the interstitial fluid flow at micro-scale and describe properly the confined transport of H_2O molecules through the channels. Pressure difference from either an atomic pressure or hydrostatic pressure gradient, is generated in MD simulation by applying an external constant force on each atom of the liquid flow and has been used to derive liquid transport in many materials, such as carbon nanotubes, graphenes, zeolites, metal-organic frames, polymers and others [26–28]. These reports reveal that the pressure difference, pore shape, pore size, temperature, hydrogen-bond (H-bond) and orientation play a vital role in diffusions and ordering of H_2O molecules. However, the structure and dynamics of confined water from bulk phase going through the seepage channel of fractured rock in grotto relics obtained from MD simulations has never been reported. The distribution, orientation and motion trajectories of H_2O molecules passing through the seepage channel are still unclear.

Because of the particularity of cultural relics, many non-destructive and in-situ methods are restricted, except for field observations [3]. Numerical modeling is the first choice for quantifying water seepage in grotto relics. In this study, we will be confining ourselves to perform FE and MD simulation targeting at visualizing the water seepage through macro-channel and micro-channel related to the direct infiltration of natural rainfall, in which an atomistic configuration of parallel feldspar-quartz platelets mimicking skeleton micro-channel was derived and then the Lennard–Jones(LJ) potentials and Einstein relations was employ, thus to provide a better understanding of the driving processes of internal water transport in grotto relics and a theoretical basis for the conservation of the World Cultural Heritage.

Geological background and simulated conditions

Geological background

Yungang Grottoes (113°20'E, 40°04'N) is located at Datong city of Shanxi Province, China, as displayed in Fig. 1. The grottoes are known as one of the largest grotto groups in China and the world-famous stone carving art, including 45 major caves, 252 shrines and approximately 51,000 sculptures. There is an average of 423 mm rain per year with rainfall distribution mostly in July, August and September. The annual average evaporation is 1748 mm, with the maximum of 801 mm in June.

The whole grottoes are divided into three parts: the east (1st–4th Cave), the middle (5th–20th Cave) and the west (21th–53th Cave). The 4th Cave with typical features of seepage hazards (Fig. 2a–f) was chosen as example of seepage channel survey where the blue box shows the actual observed water seepage and the bottom of the grottoes is 10 m higher than the groundwater level, completely in the aeration zone. Precipitation is

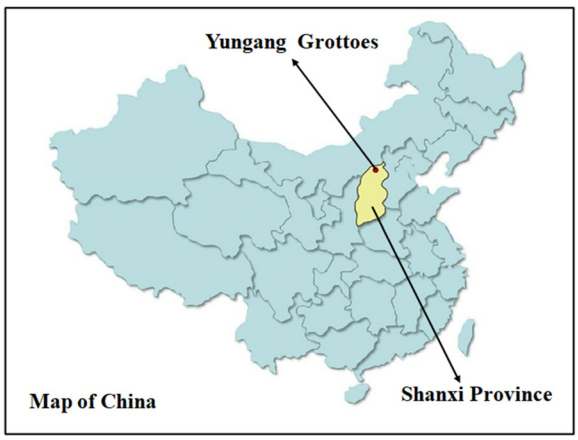

Fig. 1 The geological location of Yungang Grottoes in China

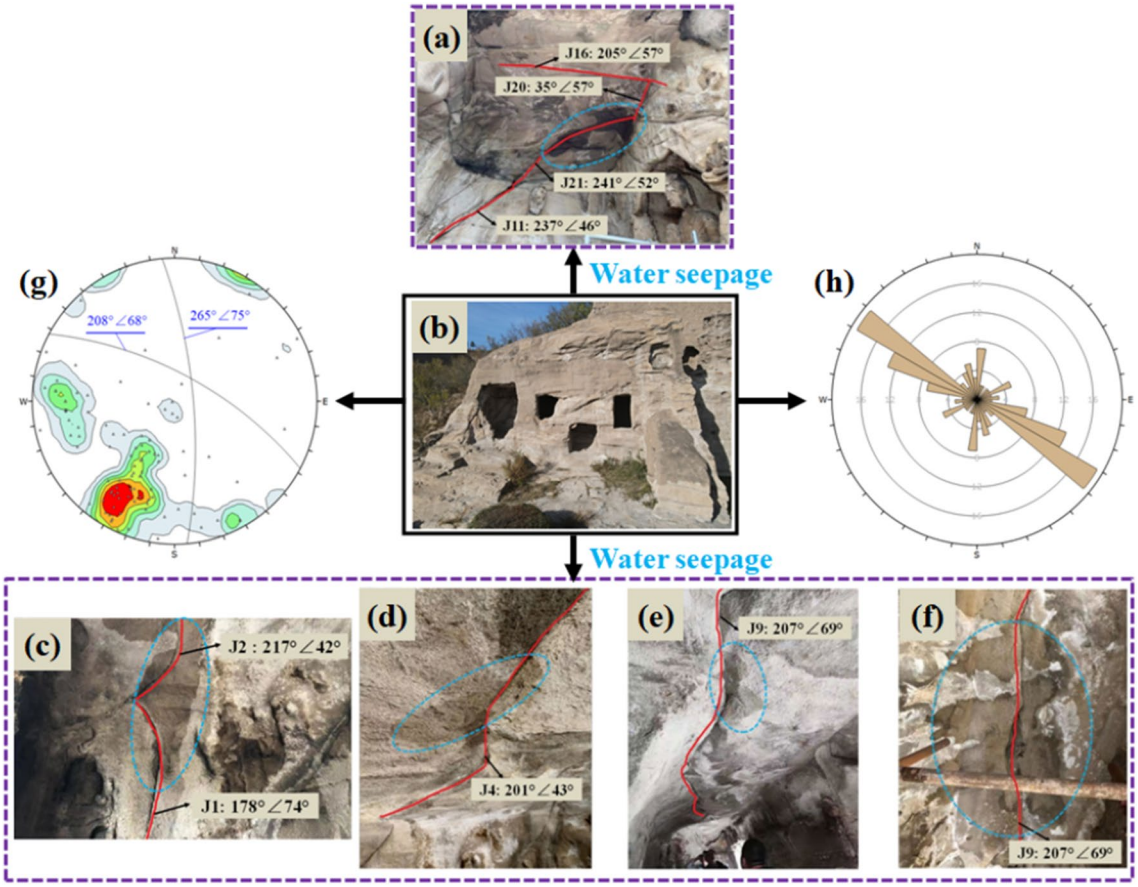

Fig. 2 **a**–**f** Representation of fractured rock mass and the water seepage phenomenon inside the 4th Cave; **c** the overview of the 4th Cave; **g** stereographic diagram for the joint trend analysis using upper hemisphere projection; **h** Rose diagram for joint pattern analysis

the only source of replenishment for groundwater, which continues seeping via fractures until arriving in groundwater. Tensile joints were the most developed joints in the east of Yungang Grottoes, appearing in groups, with dip direction nearly erect and extension direction nearly east–west, roughly parallel to the faults. A total of 97 joints inside the 4th Cave were measured and the stereographic diagram for the joint patterns analysis was displayed in Fig. 2g, using upper hemisphere projection, as evidence from the rose diagram for the joint patterns analysis in Fig. 2h. The pole of each facet was shown by a triangle and the average plane was drawn with a circle line. Two groups of the joints in the 4th Cave were obvious: one group was 208°∠68° with direction of S62°E and the other is 265°∠75°with direction of N5°W。

Measurement of chemical composition

The grotto rock powders were prepared and measured using a X-ray diffraction detector (XRD, D8 Advance) with a scanning range from 3 to 70°. The XRD patterns of the grotto rock powders were analyzed in Fig. 3a for identifying the chemical composition existed in the grotto rocks. It is characteristic of obvious peaks at 20°, 26°, 36°, 39°, 50° and 60°, which could indexed to the standard lattice parameters of quartz. The typical diffraction peaks of feldspar were displayed at 28°, 35° and 42°. The peaks at 8°, 12°, 19° and 24° indicated the existence of biotite and kaolinite. It is mainly composed of 54.39% quartz and 31.20% feldspar according to semi-quantitative calculation as illustrated in Fig. 3b and as a result, feldspar-quartz slab was generated for the current computational studies.

Computational methods and models

Finite element computational details

Various studies have shown that the critical Reynolds number (Re) for a flow between a Darcy and a non-Darcy flow is 10 and the flow satisfies Darcy`s law when $\mathrm{Re} \leq 10$ [29]. Re is defined as (Eq. 1) [30]

$$\mathrm{Re} = \frac{\rho Q}{\mu b} \tag{1}$$

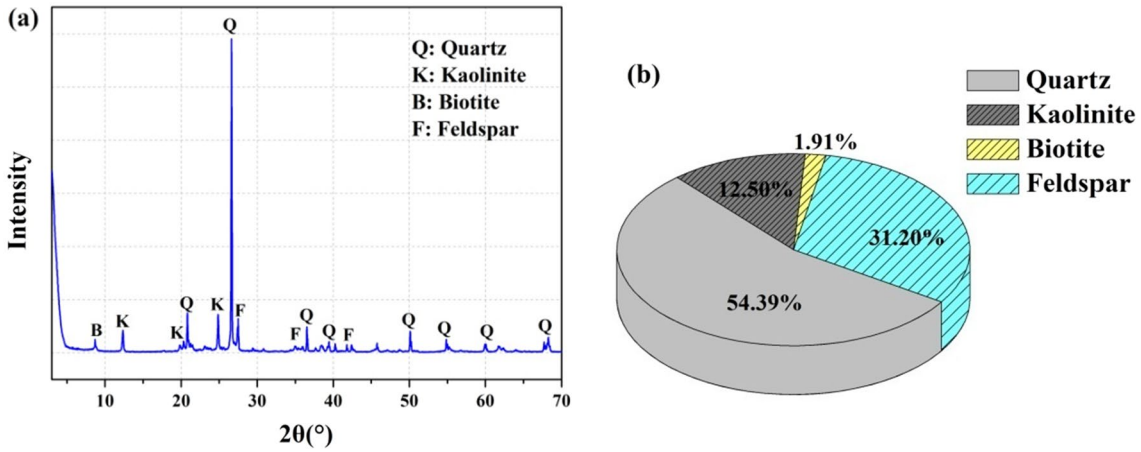

Fig. 3 **a** The XRD patterns **b** chemical composition of grotto rock

where ρ is the density of water, Q is the flow rate, μ is the viscosity of water, b is the aperture of the fracture. In this paper, ρ is 1.0×10^3 kg m^{-3}, μ is 1.005 mPa *s* [30], Q is 1.0×10^{-5}–2.0×10^{-6} m^3/s [31] and b is 0.001 m. So, the Re equals to 1.99–9.95 and it was governed by Darcy`s law.

The macro-scale FE model was conducted using commercial available ANSYS software as depicted in Fig. 4. The mesh was generated for all the volume entities with 10-node tetrahedral element to better mesh quality and the converging rate. As a consequence, the FE model was discretized using approximately 8078 tetrahedral

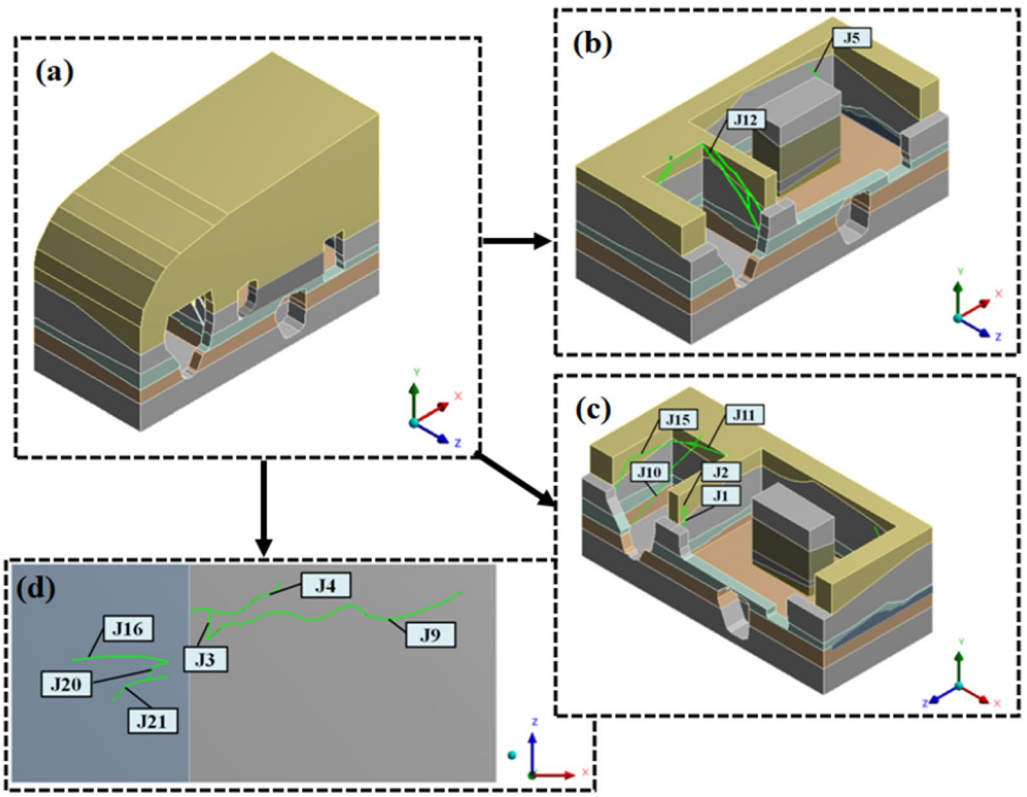

Fig. 4 The FE model from various perspectives: **a** overview; **b**, **c** section view; **d** top view

elements and 17,139 nodes. The rainfall infiltration was considered in the boundary conditions and the rainfall intensity on the top surface was set as 100 mm d^{-1}. The bottom surface was impermeable boundary. The rainfall infiltrated from the top surface to the underground and it was governed by Darcy's law (Eq. 2) [32–34]:

$$v = -k\frac{\partial h}{\partial l} \tag{2}$$

where v is the seepage rate, k is the permeability h is the total head,l is the length of seepage path.

The flow rate Q can be calculated according to Eq. 3 [32–34]:

$$Q = kw\frac{h_1 - h_2}{l} \tag{3}$$

where w is the cross-section area.

The general governing differential equation for three-dimensional seepage can be expressed mathematically as following (Eq. 4) [35]:

$$\frac{\partial}{\partial x}\left(k_x\frac{\partial h}{\partial x}\right) + \frac{\partial}{\partial y}\left(k_x\frac{\partial h}{\partial y}\right) + \frac{\partial}{\partial z}\left(k_x\frac{\partial h}{\partial z}\right) = \gamma_w m_w\frac{\partial h}{\partial t} \tag{4}$$

where k_x, k_y and k_z are the permeability in the X-, Y- and Z- direction, γ_w is the specific weight of water and m_w is storage curve slope.

MD computational details

The external pressure was applied to drive the fluid flow. All MD simulations are performed by Accerlery Materials Studio software. Figure 5 depicts the initial configuration of parallel feldspar-quartz slabs mimicking skeleton nanochannel with the inter-space (d) of 2.0 nm. A simple point charge-extended (SPC/E) model was applied for H_2O molecules because of its excellent description for bulky water. 737 H_2O molecules with density equal to = 1.0 g/cm^{-3} was randomly filled into the left reservoir with dimension of $2.00 \times 2.51 \times 4.40$ nm^3. The model consists of a 3×2 supercell of quartz slab and a 8×5 supercell of feldspar slab, for which position constraints were employed. One-layer Graphene sheet with size of 2.46×5.04 nm^2 is assigned to motion group and acts as moveable wall (piston) for creating the driven force toward H_2O molecules in the left reservoir and the right reservoir ($2.00 \times 2.51 \times 4.40$ nm^3) was kept empty. Geometry optimization of 5,000 iterations was achieved for energy minimization. Following this, a MD simulation via the isothermal-isometric(NVT) ensemble with the Nose thermostat is performed using Drieding force field at 298 K with a timestep of 1 fs. The intermolecular

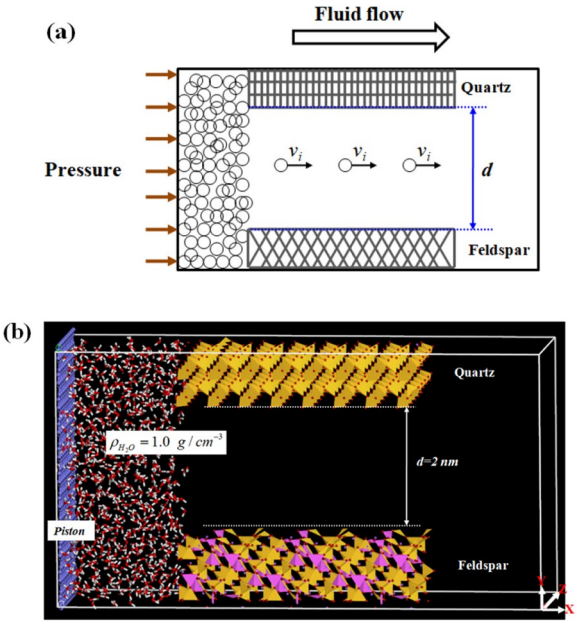

Fig. 5 **a** The schematic diagram of pressure-driven fluid flow in seepage channel and **b** the specification of the system employed in our study to analyze the transport properties of H_2O molecules through seepage channel of fractured rock in grotto relics

potential energy includes the LJ 6–12 type potential (E_{vdW}) and the Coulomb potential (E_{ele}) to describe van der Waals and electrostatic interactions, respectively. Their mathematical expressions are displayed in Eq. 5 [36].

$$U(r) = E_{vdW} + E_{ele} = 4\varepsilon\left[\left(\frac{\sigma}{r_{ij}}\right)^{12} - \left(\frac{\sigma}{r_{ij}}\right)^{6}\right] + \frac{e^2}{4\pi\varepsilon_0}\sum_{i\neq j}\frac{q_i q_j}{r_{ij}} \tag{5}$$

The LJ parameters for the O atoms are $\sigma = 0.354$ nm and $\varepsilon = 0.152$ kcal/*mol*[36].

Results and discussions

The main source of the seepage water in the grottoes was the rainfall infiltration and seepage recharge through joint fissures or joint fractures, mainly depending on the rainfall intensity and permeability [37]. The seepage field calculated from FE method was displayed in the form of color-coded contours of the water head and flow rate distribution in response to the rainfall intensity of 100 mm d^{-1} (Fig. 6). Joints with a direction of S62°E were recognized to be an effective channel for water seepage. In the fracture zone, water infiltrates quickly from the top surface into the joint fracture with a high value of water heads, in accordance with the actual seepage

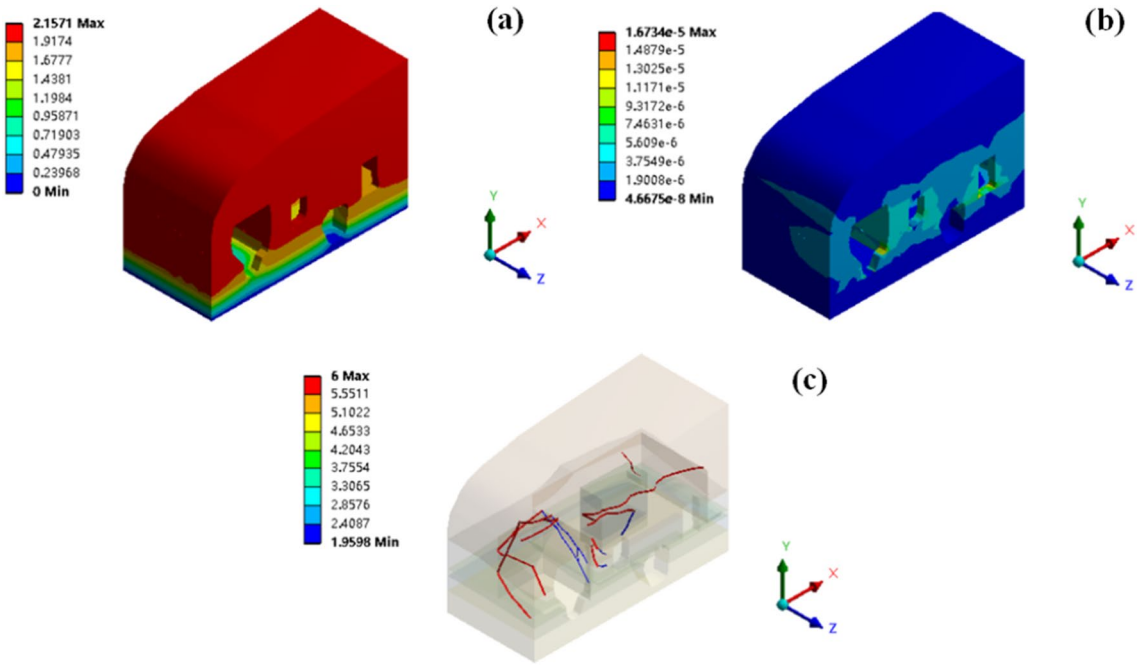

Fig. 6 The seepage field calculated from FE method under rainfall intensity of 100 mm d^{-1}: **a** water head (*m*) contours of the 4th cave; **b** the flow rate ($m^3 \cdot s^{-1}$) contours of the 4th cave; **c** water head (*m*) contours of joint fissures

point in Fig. 2a–f, where the flow rate was ranging from 1.67×10^{-5} to 4.67×10^{-8} m^3 s^{-1}. The direct infiltration of natural rainfall acted as the driving force of water migration, providing a framework to construct an atomic model of the pore flow in the subsequent section.

The flow direction of water seepage is generally from the low potential area to the high potential area. H_2O molecules suffered from a large energy barrier and they should overcome the large occupancy fluctuations to occupy the empty vacancies, which comes from larger energy barrier with strong interactions between water and channel. Figure 7a displayed the time course of energy variation evolving potential energy and its components during NVT simulation. It is found that they showed stable energy levels, a relatively strong electrostatic interaction (attractive) and a relatively weak van der Waal (vdW) interaction (repulsive), leading to a high potential energy barrier. Figure 7b illustrated the variation in the number of H_2O molecules entering into seepage channel versus time. The water occupancy increased

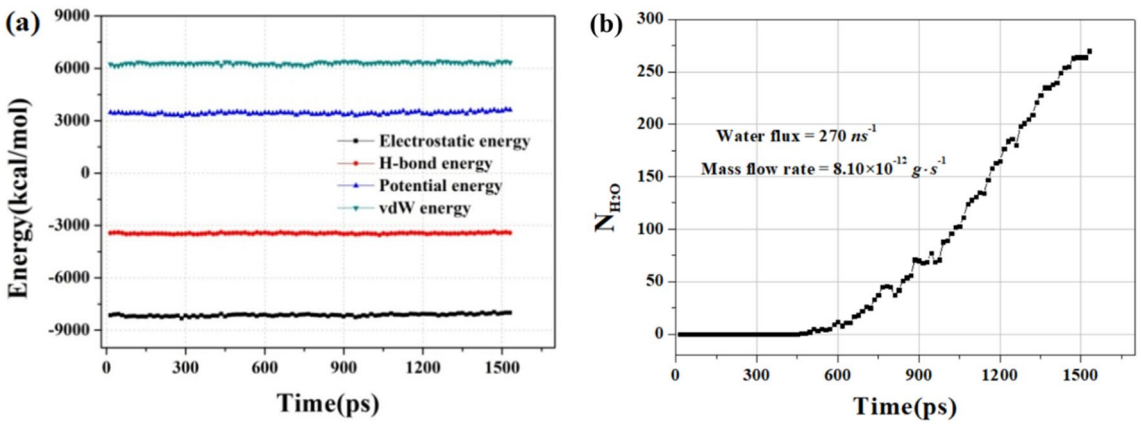

Fig. 7 **a** The time course of energy variation during NVT simulation and **b** the number of H_2O molecules transported through the seepage channel depicted as a function of simulation time

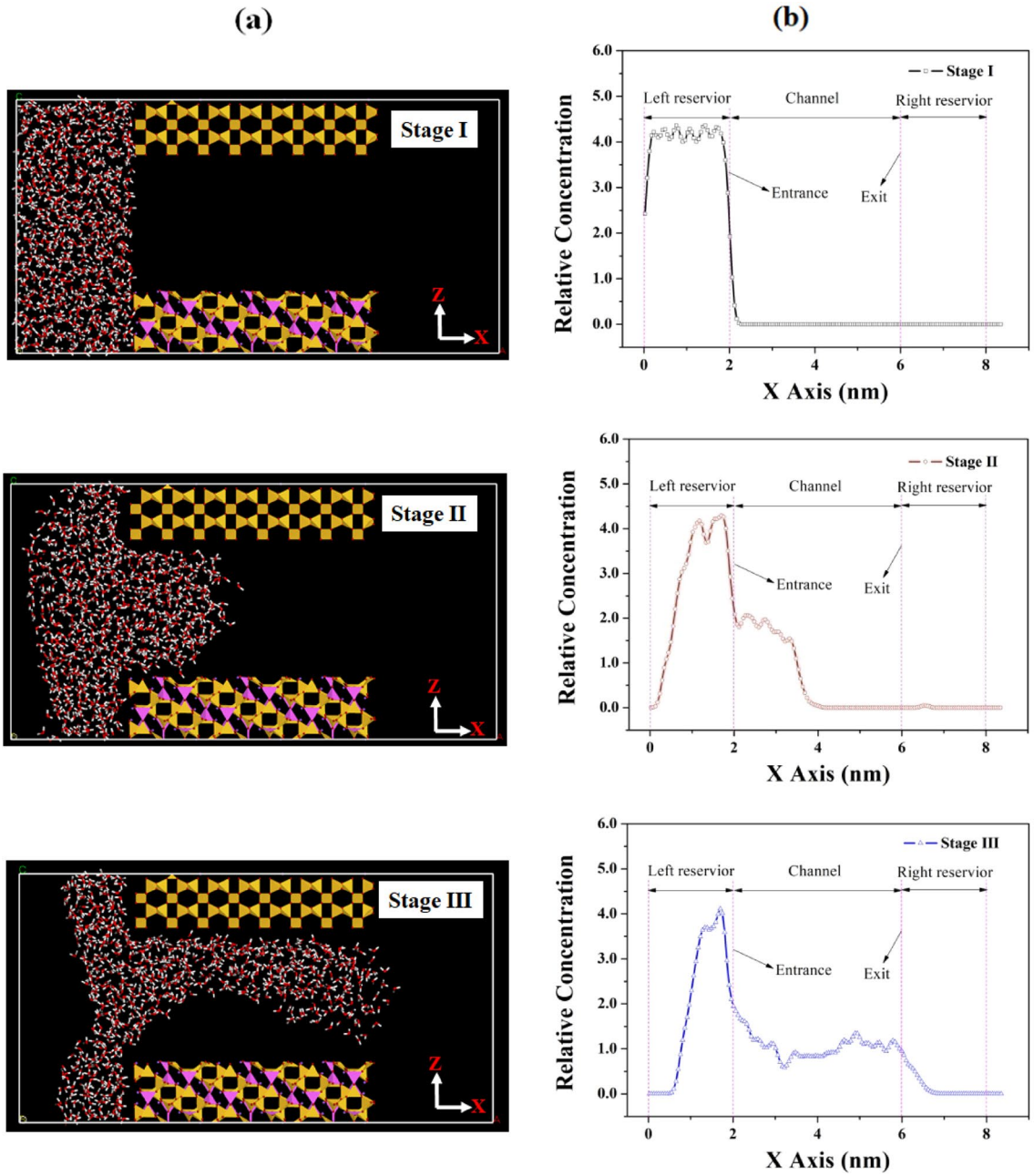

Fig. 8 **a** The cross-sectional snapshots of H_2O molecules configurations through the seepage channel from the left reservoir at various stages and **b** the related concentration profiles along *X* -axis direction

monotonously with simulation time. During the whole simulation time, there were 270 H_2O molecules passing through channel from the initial position along the flow direction, from which the water flux and mass flow rate can be calculated [26, 38], equal to 270 ns^{-1} and 8.10×10^{-12} g s^{-1}, respectively. The magnitude of mass flow rate was close to the mass flow rate of graphene-based nanochannel with the pore width of 0.7–1 nm [28].

The flow behavior of H_2O molecules in seepage channel involved three steps: (1) permeate into the seepage channel; (2) moving along the channel; (3) flow out of the channel. In order to probe the transport phenomena in detail, three stages (stage I, stage II and stage III) were defined as clarification of H_2O molecules in the entrance region, the center region and the exit region, respectively. The typical feature at various stages was demonstrated

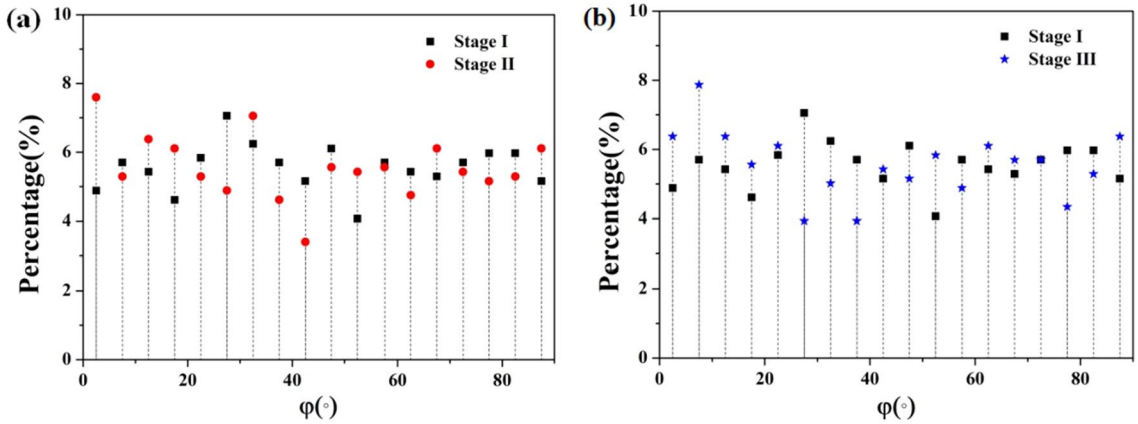

Fig. 9 The orientation distribution of H_2O molecules in *XZ* plane at the various stages: **a** comparison of stage I and stage II; comparison of stage I and stage III

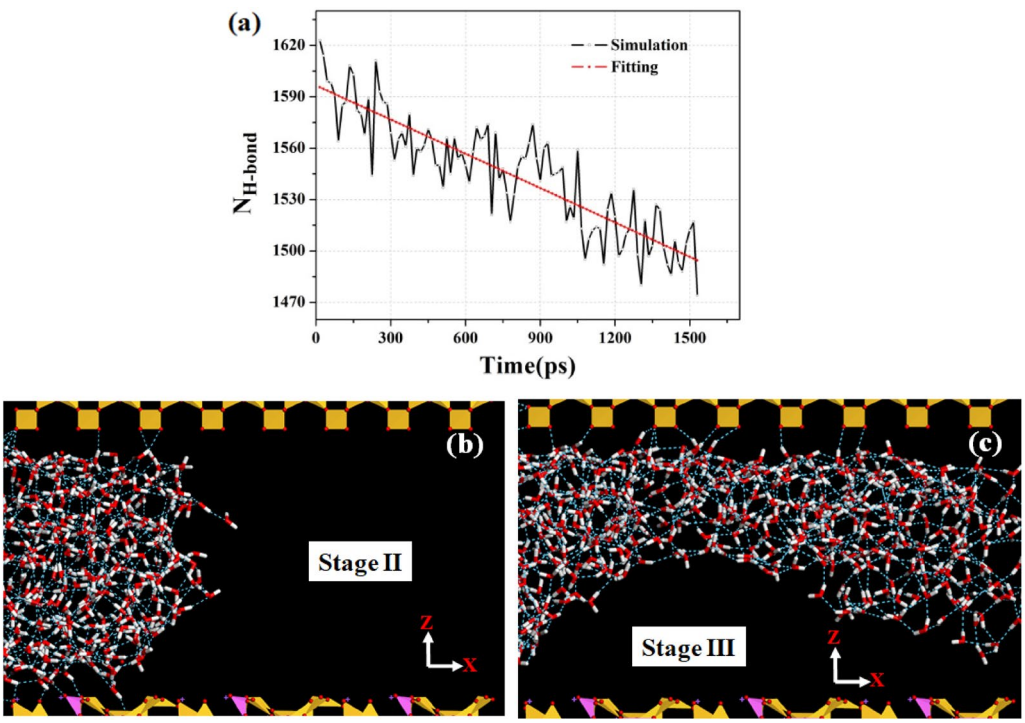

Fig. 10 **a** The number of H-bonds depicted as a function of simulation time and **b**, **c** the cross-sectional snapshots at stage II and stage III

in Fig. 8a, giving a dynamic process of water transport from the entrance region to the exit region. We divided the simulation box into many slabs along *X*-axis direction for statistical analysis. Hence, the relative concentration is given by the ratio of concentration in the slab to its average concentration across the entire system, as demonstrated in Fig. 8b. Significant discrepancies emerge at the number and magnitude of the peak values existing in the relative concentration distribution curve. Specifically, at stage I, H_2O molecules are uniformly dispersed in the left reservoir with uniform distribution as verified by the multi-peaks. Part of H_2O molecules entered into the channel because the relative concentration in the range of 2–4 *nm* changed from 0 to 2.0, as can be seen at stage II. When the whole channel was filled by H_2O molecules, the relative concentration among the channel fluctuated around 1.0, indicating a uniform distribution at stage III.

These findings are consistent with the morphologies shown in Fig. 8a.

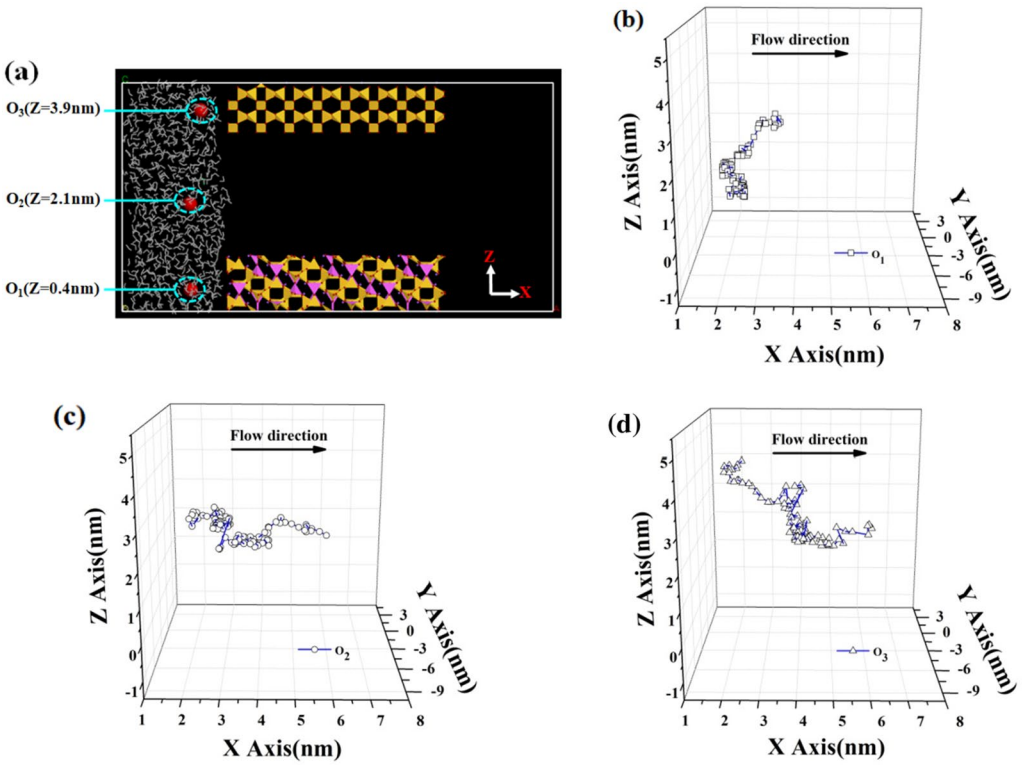

Fig. 11 **a** The O_n (n = 1, 2, 3) diagram in H_2O molecules located at different position along *Z*-axis direction and **b**–**d** the moving trajectories of O_1, O_2 and O_3

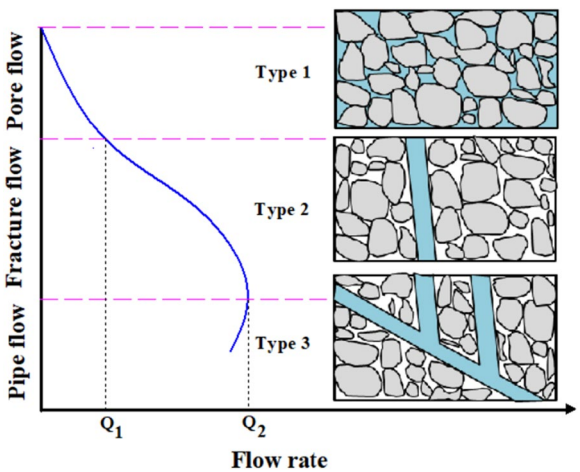

Fig. 12 Three types of water seepage in grotto relics

The orientation distribution of O–H bonds in H_2O molecules in a specified stage was also obtained to gain insight into ordering of the confined water, as plotted in Fig. 9. The orientation was defined as the angle between the flow direction (*X*-axis) and O–H bonds in H_2O molecules. We have also included the corresponding orientation distribution at each stage for comparison. As can be seen, for each stage, there was a broader angular distribution and no ordered configuration, suggesting that the orientation behavior of confined H_2O molecules responded to pressure-driven flow field without any disruption. The various distributions of may be derived from the fluctuation of H_2O molecules and random thermal motion [39]. It was unfavorable for forming H-bonds among confined H_2O molecules. A detailed discussion on the H-bond inspection is presented in the following section.

The aforementioned orientation behavior may be relevant to the H-bonds formation. When the H_2O molecules orient themselves parallel to the flow direction, it is in favor of the formation of H-bonds among the confined H_2O molecule. For a more detailed discussion, the number and structure of H-bonds for confined H_2O molecules were characterized, as shown in Fig. 10. When the distance between the O atom of one H_2O molecule, and the H atom of another H_2O molecule was less than 3.0 Å, one can assume that a H-bond was formed [18, 40]. Having a precise look at Fig. 10, it has experienced a nearly decreasing trend in the number of H-bonds with ignorance of some fluctuations. The H_2O molecules should break some of H-bonds to enter the narrow channel due

to steric crowding and large energy barrier, leaving a reduction in the number of H-bonds. This finding agrees well with the results of orientation distribution O–H bonds in H_2O molecules. In addition, it is further interpreted as the strong repulse interaction between H_2O molecules and feldspar because some reduction has been occurred may be attributed to the disappearance of the H-bonds between H_2O molecules and feldspar surface (see Fig. 10c).

Besides analyzing the energy variation, water flux, relative concentration profiles, orientation distribution and H-bonds, further analysis is here focused on describing motion trajectories for elucidating the flow mechanism, by depicting the Cartier coordinates (x, y, z) of O atoms in H_2O molecules located at different position along Z -axis direction. Figure 11a gives their initial positions of O_n (n = 1, 2, 3). The moving trajectories of O_1, O_2 and O_3 in X-, Y- and Z-axis directions were extracted and exhibited in Fig. 11b–d. What is worth mentioning is that the tagged O atoms experienced a zigzag movement instead of linear motion as expected, roughly exhibited the same target direction, moving towards the exit.

The seepage characteristics in grotto relics experienced a complex evolution process and three types can be summarized as water seepage propagation behavior in grotto relics (see Fig. 12): for type 1, the pores interconnected with other pores to form micro-channels and water infiltrates through micro-channels of fracture zone or the small original cracks in the upper area, where the flow rate is low. As a result of washout of atmospheric rainfall, water flows through fracture with a relatively high flow rate (type 2). With the expanding and connecting of fracture or cracks, water seepage maybe turned into a kind of analogous pipe flow, resulting in water seepage hazards (type 3).

Conclusions

In this study, a new attempt was made to employ FE and MD simulations for elucidating the water infiltration and seepage characteristics through the macro-channel and micro-channel of fractured rock in grotto relics in consideration of the rainfall infiltration. The feldspar-quartz slab was generated for MD simulation because it is mainly composed of 54.39% quartz and 31.20% feldspar in grotto rock, as verified by XRD patterns. The water occupancy increased monotonously with simulation time and there were 270 H_2O molecules passing through channel from the initial position along the flow direction, from which the water flux and mass flow rate were calculated. It is found that the broader angular distribution and disordered configuration existed in confined H_2O molecules was unfavorable for forming H-bonds among confined H_2O molecules, which was verified by the H-bond analysis. The motion trajectories of H_2O molecules along Z-direction were investigated and they showed a zigzag movement instead of linear motion as expected. Three types can be summarized as water seepage propagation behavior in grotto relics: for type 1, the pores interconnected with other pores to form micro-channels and water infiltrates through micro-channels in the upper area with a low flow rate; for type 2, water flows through fracture with a relatively high flow rate; for type 3, it turned into a kind of analogous pipe flow as the expanding and connecting of fracture or cracks, resulting in water seepage hazard.

Abbreviations

XRD	X-ray diffraction
UNESCO	The United Nations Educational, Scientific and Cultural Organization
FE	Finite element
FD	Finite difference
MD	Molecular dynamics
H-bond	Hydrogen-bond
LJ	Lennard–Jones
v	The seepage rate
k	The permeability
h	The total head
l	The length of seepage path
Q	Flow rate
w	The cross-section area
k_x, k_y, k_z	The permeability in the X-, Y- and Z- direction
γ_w	The specific weight of water
m_w	Storage curve slope
SPC/E	Simple point charge-extended
NVT	Isothermal-isometric
vdW	Van der Waal

Acknowledgements

We acknowledge the Administrative Center for China's Agenda 21, Fudan University, Shanxi culture relics bureau and the Research Institute of Yungang.

Author contributions

JW participated in the design o the study, carried out all the analyses and drafted the manuscript. The author read and approved the final manuscript.

Funding

The research was supported by National Key R&D Program of China (2021YFC1523400) and the science and technology project for cultural relic conservation of Shanxi culture relics bureau (208141400237).

Availability of data and materials

Data was available on request from the author.

Declarations

Competing interests

The authors declare no competing interests.

Received: 2 August 2022 Accepted: 17 November 2022
Published online: 09 January 2023

References

1. Meng T, Du R, Hou Z, Yang J, Zhao G. THz spectra-based SVM prediction model for Yungang Grottoes samples. J Archaeol Sci. 2015;55:280–5. https://doi.org/10.1016/j.jas.2015.01.012.

2. Wang XS, Wan L, Huang J, Cao W, Xu F, Dong P. Variable temperature and moisture conditions in Yungang Grottoes, China, and their impacts on ancient sculptures. Environ Earth Sci. 2014;72(8):3079–88. https://doi.org/10.1007/s12665-014-3213-x.
3. Zhang J, Li Z, Li L, Liu J, Liu D, Shao M. Study on weathering mechanism of sandstone statues in Southwest China: example from the sandstone of niche of sakyamuni entering nirvana at dazu rock carvings. Nat Hazards. 2021;108(1):775–97. https://doi.org/10.1007/s11069-021-04705-w.
4. Liu RZ, Zhang BJ, Zhang H, Shi MF. Deterioration of Yungang Grottoes: diagnosis and research. J Cult Herit. 2011;12(4):494–9. https://doi.org/10.1016/j.culher.2011.03.008.
5. Guo F, Jiang G. Investigation into rock moisture and salinity regimes: implications of sandstone weathering in Yungang Grottoes. China Carbonate Evaporite. 2014;30(1):1–11. https://doi.org/10.1007/s13146-014-0191-8.
6. Meng T, Lu Y, Zhao G, Yang C, Ren J, Shi Y. A synthetic approach to weathering degree classification of stone relics case study of the Yungang Grottoes. Herit Sci. 2018;6:1. https://doi.org/10.1186/s40494-017-0165-y.
7. Yang X, Wang J, Zhu C, He M. Effect of water on long-term strength of column rocks based on creep behavior in Yungang Grottoes. China Geotech Geol Eng. 2018;37(1):173–83. https://doi.org/10.1007/s10706-018-0601-0.
8. Geng H, Zhang S, Zhi J, Zhang R, Ren J, Ro C-U. Acid solution decreases the compressional wave velocity of sandstone from the Yungang Grottoes, datong. China Herit Sci. 2019;7:4. https://doi.org/10.1186/s40494-019-0245-2.
9. Qin Y, Wang Y, Li L, Huang J. Experimental weathering of weak sandstone without direct water participation by using sandstone from the Yungang Grottoes in Datong. China Rock Mech Rock Eng. 2016;49(11):4473–8. https://doi.org/10.1007/s00603-016-1003-3.
10. Li H, Wang W, Zhan H, Qiu F, Guo Q, Zhang G. Water in the mogao grottoes, China: where it comes from and how it is driven. J Arid Land. 2014;7(1):37–45. https://doi.org/10.1007/s40333-014-0072-y.
11. Lu K, Li Z, Niu R, et al. Using surface nuclear magnetic resonance and spontaneous potential to investigate the source of water seepage in the JinDeng temple grottoes. China J Cult Herit. 2020;45:142–51. https://doi.org/10.1016/j.culher.2020.05.006.
12. Shi C, Zhang W, Chen X, Wang L. Seepage deformation and failure of rock mass under high water pressure with a discrete element method. Front Phys. 2022;10:857158. https://doi.org/10.3389/fphy.2022.857158.
13. Di K, Li M, Mao X, et al. Experimental study of the water-sediment two-phase seepage characteristics in rock fractures and the influencing factors. Geofluids. 2021;2021:1–14. https://doi.org/10.1155/2021/9808238.
14. Zhang M, Chang C, Cao W. A discussion of reinforcement timing optimization for main inclined shaft roadway with water seepage. Geofluids. 2020;2020:1–8. https://doi.org/10.1155/2020/8850911.
15. Lv X, Wang Z, Wang J. Seepage–damage coupling study of the stability of water-filled dump slope. Eng Anal Bound Elem. 2014;42:77–83. https://doi.org/10.1016/j.enganabound.2013.08.010.
16. Li S, Jiang Z, Que Y, et al. Water field distribution characteristics under slope runoff and seepage coupled effect based on the finite element method. Water. 2021;13:24. https://doi.org/10.3390/w13243569.
17. Hadidi H, Kamali R. Non-equilibrium molecular dynamics simulations of water transport through plate- and hourglass-shaped CNTs in the presence of pressure difference and electric field. Comp Mater Sci. 2020;185:109978. https://doi.org/10.1016/j.commatsci.2020.109978.
18. Richard R, Anthony S, Aziz G. Pressure-driven molecular dynamics simulations of water transport through a hydrophilic nanochannel. Mol Phys. 2016;114(18):2655–63. https://doi.org/10.1080/00268976.2016.1170219.
19. Vijayaraghavan V, Wong CH. Transport characteristics of water molecules in carbon nanotubes investigated by using molecular dynamics simulation. Comp Mater Sci. 2014;89:36–44. https://doi.org/10.1016/j.commatsci.2014.03.025.
20. Wang L, Dumont RS, Dickson JM. Nonequilibrium molecular dynamics simulation of pressure-driven water transport through modified CNT membranes. J Chem Phys. 2013;138(12):124701. https://doi.org/10.1063/1.4794685.
21. Wu HC, Yoshioka T, Nakagawa K, Shintani T, Saeki D, Matsuyama H. Molecular simulation of a modified amphotericin B-Ergosterol artificial water channel to evaluate structure and water molecule transport performance. J Membrane Sci. 2019;583:49–58. https://doi.org/10.1016/j.memsci.2019.04.021.
22. Wu HC, Yoshioka T, Nakagawa K. Water transport and ion rejection investigation for application of cyclic peptide nanotubes to forward osmosis process: a simulation study. Desalination. 2017;424:85–94. https://doi.org/10.1016/j.desal.2017.09.008.
23. Wang L, Dumont RS, Dickson JM. Nonequilibrium molecular dynamics simulation for studying the effect of pressure difference and periodic boundary conditions on water transport through a CNT membrane. Mol Phys. 2017;115(8):981–90. https://doi.org/10.1080/00268976.2017.1298862.
24. Han KN, Bernardi S, Wang L, Searles DJ. Water structure and transport in zeolites with pores in one or three dimensions from molecular dynamics simulations. J Phys Chem C. 2017;121(1):381–91. https://doi.org/10.1021/acs.jpcc.6b10316.
25. Sohrevardi N, Bozorgmehr MR, Heravi MM, Khanpour M. Transport properties of mixtures composed of acetone, water, and supercritical carbon dioxide by molecular dynamics simulation. J Supercrit Fluid. 2017;130:321–6. https://doi.org/10.1016/j.supflu.2017.06.017.
26. Docherty SY, Nicholls WD, Borg MK, Lockerby DA, Reese JM. Boundary conditions for molecular dynamics simulations of water transport through nanotubes. J Mech Eng Sci. 2013;228(1):186–95. https://doi.org/10.1177/0954406213481760.
27. Wang L, Dumont RS, Dickson JM. Molecular dynamic simulations of pressure-driven water transport through polyamide nanofiltration membranes at different membrane densities. RSC Adv. 2016;6(68):63586–96. https://doi.org/10.1039/c6ra12115b.
28. Yang X, Yang X, Liu S. Molecular dynamics simulation of water transport through graphene-based nanopores: flow behavior and structure characteristics. Chin J Chem Eng. 2015;23(10):1587–92. https://doi.org/10.1016/j.cjche.2015.05.015.
29. Liu J, Chen W, Liu T, Yu J, Dong J, Nie W. Effects of initial porosity and water pressure on seepage-erosion properties of water inrush in completely weathered granite. Geofluids. 2018;2018:1–11. https://doi.org/10.1155/2018/4103645.
30. Liu Y, Li S. Influence of particle size on non-darcy seepage of water and sediment in fractured rock. Springerplus. 2016;5(1):2099. https://doi.org/10.1186/s40064-016-3778-9.
31. Wang JH, Ren WZ, Liu B. Study on the mechanism of water seepage in the cliff statues of dazu rock cavings. Wuhan: China University of Geosciences Press; 2019.
32. Meng FQ. Numerical simulation with ANSYS on stable seepage field of earth rock-fill dam. Dalian: Dalian Univeristy of Technology; 2005.
33. Sun WJ. Earth-rock dam seepage analysis and research base with ANSYS thermal analysis module. Zhenzhou: North China University of Water Resources and Electric Power; 2016.
34. Zhang YY. The application and study of ANSYS on seepager field, stress field and coupling analysis for earth dam. Nanjing: Hohai University; 2006.
35. Beiranvand B, Komasi M. An Investigation on performance of the cut off wall and numerical analysis of seepage and pore water pressure of Eyvashan earth dam. IJST-T Civ Eng. 2021;45(3):1723–36. https://doi.org/10.1007/s40996-021-00613-y.
36. Lu D. Accelerating water transport through a charged SWCNT: a molecular dynamics simulation. Phys Chem Chem Phys. 2013;15(34):14447–57. https://doi.org/10.1039/c3cp51855h.
37. Fang S, Zhang B, Zhang K. The long-term monitoring and evaluation of cement-based grout used to govern the water seepage of karst caves in China. Herit Sci. 2020;8:50. https://doi.org/10.1186/s40494-020-00392-1.
38. Han C, Tang D, Kim D. Molecular dynamics simulation on the effect of pore hydrophobicity on water transport through aquaporin-mimic nanopores. Colloid Surface A. 2015;481:38–42. https://doi.org/10.1016/j.colsurfa.2015.04.012.
39. Song Y, Wei M, Xu F, Wang Y. Molecular simulations of water transport resistance in polyamide ro membranes: interfacial and interior

contributions. Engineering. 2020;6(5):577–84. https://doi.org/10.1016/j.eng.2020.03.008.
40. Shahbabaei M, Kim D. Molecular simulation study of water transport through aquaporin-inspired pore geometry. J Mech Sci Technol. 2017;31(8):3845–51. https://doi.org/10.1007/s12206-017-0729-5.

Publisher's Note